

# Fundamental activity constraints lead to specific interpretations of the connectome

Jannis Schuecker<sup>1,\*</sup>, Maximilian Schmidt<sup>1,\*</sup>, Sacha J. van Albada<sup>1</sup>, Markus Diesmann<sup>1,2,3</sup>, and Moritz Helias<sup>1,3</sup>

<sup>1</sup>Institute of Neuroscience and Medicine (INM-6) and Institute for Advanced Simulation (IAS-6) and JARA BRAIN Institute I, Jülich Research Centre, 52428 Jülich, Germany

<sup>2</sup>Department of Psychiatry, Psychotherapy and Psychosomatics, Medical Faculty, RWTH Aachen University, 52062 Aachen, Germany

<sup>3</sup>Department of Physics, Faculty 1, RWTH Aachen University, 52062 Aachen, Germany

\*Both authors contributed equally to this work.

arXiv:1509.03162v2 [q-bio.NC] 19 Feb 2016

Correspondence to: Jannis Schuecker, Wilhelm-Johnen-Straße, 52425 Jülich  
j.schuecker@fz-juelich.de

## Acknowledgements

The authors gratefully acknowledge the computing time granted by the JARA-HPC Vergabegremium and provided on the JARA-HPC Partition part of the supercomputer JUQUEEN (Jülich Supercomputing Centre, 2015) at Forschungszentrum Jülich. Partly supported by Helmholtz Portfolio Supercomputing and Modeling for the Human Brain (SMHB), the Helmholtz young investigator group VH-NG-1028, EU Grant 269921 (BrainScaleS), and EU Grant 604102 (Human Brain Project, HBP). All network simulations carried out with NEST (<http://www.nest-simulator.org>).

## Abstract

The continuous integration of experimental data into coherent models of the brain is an increasing challenge of modern neuroscience. Such models provide a bridge between structure and activity, and identify the mechanisms giving rise to experimental observations. Nevertheless, structurally realistic network models of spiking neurons are necessarily underconstrained even if experimental data on brain connectivity are incorporated to the best of our knowledge. Guided by physiological observations, any model must therefore explore the parameter ranges within the uncertainty of the data. Based on simulation results alone, however, the mechanisms underlying stable and physiologically realistic activity often remain obscure. We here employ a mean-field reduction of the dynamics, which allows us to include activity constraints into the process of model construction. We shape the phase space of a multi-scale network model of primate visual cortex by systematically refining its connectivity. Fundamental constraints on the activity, i.e., prohibiting quiescence and requiring global stability, prove sufficient to obtain realistic layer- and area-specific activity. Only minimal adaptations of the structure are required, showing that the network operates close to an instability. The procedure identifies components of the network critical to its collective dynamics and creates hypotheses for structural data and future experiments.

## Significance statement

The connectome describes the wiring patterns of the neurons in the brain, which form the substrate guiding activity through the network. The influence of its constituents on the dynamics is a central topic in systems neuroscience. We here investigate the critical role of specific structural links between neuronal populations for the global stability of cortex and elucidate the relation between anatomical structure and experimentally observed activity. Our novel framework enables the evaluation of the rapidly growing body of connectivity data on the basis of fundamental constraints on brain activity and the combination of anatomical and physiological data to form a consistent picture of cortical networks.

## Introduction

The neural wiring diagram, the connectome, is gradually being filled through classical techniques combined with innovative quantitative analyses (Markov et al., 2014a,b) and new technologies (Wedeen et al., 2008; Axer et al., 2011). The connectivity between neurons is considered to shape resting-state and task-related collective activity (Cole et al., 2014; Shen et al., 2015). For simple networks, clear relationships with activity are known analytically, e.g., a dynamic balance between excitatory and inhibitory inputs in inhibition-dominated random networks leads to an asynchronous and irregular state (van Vreeswijk & Sompolinsky, 1996; Amit & Brunel, 1997a). Structures and mechanisms underlying large-scale interactions have been identified by means of dynamical models (Deco & Jirsa, 2012; Cabral et al., 2014) and graph theory (Markov et al., 2013; Goulas et al., 2014). Furthermore, the impact of local network

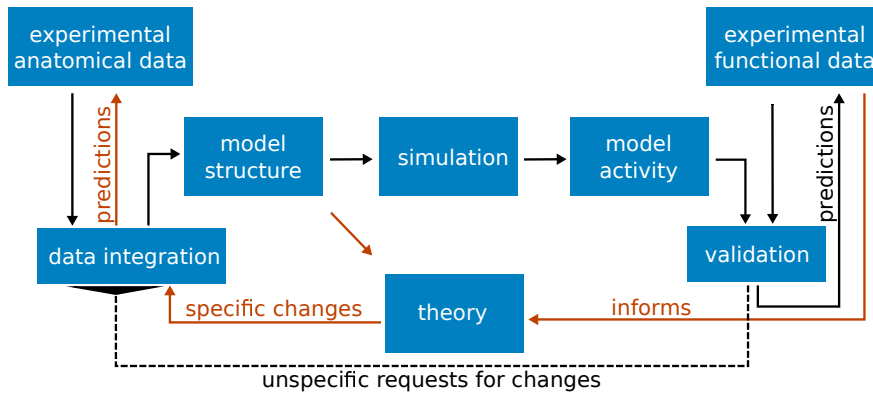
structure on spike-time correlations is known in some detail (Ostojic et al., 2009; Pernice et al., 2011; Trousdale et al., 2012). Under certain conditions, there is a one-to-one mapping between correlations in neuronal network activity and effective connectivity, a measure that depends on the network structure and on its activity (van Albada et al., 2015). In conclusion, anatomy does not uniquely determine dynamics, but dynamical observations help constrain the underlying anatomy. Despite advances in understanding simple networks, a complete picture of the relationship between structure and dynamics remains elusive.

Fig. 1 visualizes the integrative loop between experiment, model, and theory that guides the investigation of structure and dynamics. In the traditional forward modeling approach, structural data from experimental studies determine the connectivity between model neurons. Combined with the specification of the single-neuron dynamics and synaptic interactions, simulations yield a certain network dynamics. There is a fundamental problem with this approach.

Despite the impressive experimental progress in determining network parameters, any neural network model is underdetermined, because of the sheer complexity of brain tissue and inevitable uncertainties in the data. For instance, counting synapses on a large scale presently takes a prohibitive amount of time, and no available technique allows determining precise synaptic weights for entire neural populations. Although it may be possible to quantify the full connectome of an individual in future, inter-individual variability will require modelers to express connectivity as connection probabilities or rules of self-organization if they want to learn about general principles of the brain. In modeling studies, parameters are usually tuned manually to achieve a satisfactory state of activity, which becomes unfeasible for high-dimensional models due to the size of the parameter space. In particular, it is a priori unclear how parameters of the model influence its activity. In consequence, modifications cannot be performed in a targeted fashion, and it is difficult to find a minimal set of modifications necessary for aligning a model with experimental activity data.

Overcoming this problem requires a shift of perspective. Instead of regarding the model exclusively in a forward manner, generating predicted activity from structure, we in addition consider the system in a reverse manner, predicting the structure necessary to explain the observed activity. Our theory, starting from a mean-field description, provides a direct link between structure and activity. In contrast to simulations, the theory is invertible, which we exploit to identify connections critical for the dynamics and to find a minimal set of modifications to the structure yielding a realistic set point of activity. The predicted alterations generate hypotheses on brain structure, thus feeding back to anatomical experiments.

Applying the method to a multi-scale network model of macaque visual cortex, we derive targeted modifications of a set of critical connections, bringing the model closer to experimental observations of cortical activity. Based on the global properties of the bistable phase space of the model, the method refines the model's construction principles within experimental uncertainties and identifies the connections that decisively shape the dynamics. Preliminary results have been presented in abstract form (Schmidt et al., 2015b).



**Figure 1 The integrative loop between experiment, model, and theory.** Black arrows represent the classical forward modeling approach: Experimental anatomical data are integrated into a model structure, which gives rise to the activity via simulation. The model activity is compared with experimental functional data. The usual case of disagreement leads to the need to change the model definition. By experience and intuition the researcher identifies the parameters to be changed, proceeding in an iterative fashion. Once the model agrees well with a number of experimental findings, it may also generate predictions on the outcome of new experiments. Red arrows symbolize our new approach: informed by functional data, an analytical theory of the model identifies critical connections to be modified, refining the integration of data into a consistent model structure and generating predictions for anatomical studies.

## Materials and Methods

Consider a neuronal network of leaky integrate-and-fire model neurons with exponentially decaying post-synaptic currents. In the diffusion approximation, the dynamics of the membrane potential  $V$  and synaptic current  $I_s$  is (Fourcaud & Brunel, 2002)

$$\begin{aligned}\tau_m \frac{dV}{dt} &= -V + I_s(t) \\ \tau_s \frac{dI_s}{dt} &= -I_s + \mu + \sigma \sqrt{\tau_m} \xi(t),\end{aligned}\tag{1}$$

where  $\tau_m$  is the membrane time constant and  $\tau_s$  the synaptic time constant, respectively. The membrane resistance has been absorbed into the definition of the current. The input spike trains are approximated by a current which fluctuates with variance  $\sigma^2$  around the mean value  $\mu$  where the noise fluctuations are drawn from a Gaussian process  $\xi(t)$  satisfying  $\langle \xi(t) \rangle = 0$  and  $\langle \xi(t)\xi(t') \rangle = \delta(t - t')$ . Whenever the membrane potential  $V$  crosses the threshold  $\theta$ , the neuron emits a spike and  $V$  is set to the reset potential  $V_r$ , where it is clamped during  $\tau_r$ . In the networks we consider, the neurons are structured into  $N$  populations interconnected with a connectivity matrix  $\mathbf{W} = \mathbf{K} \circledast \mathbf{J}$ , where  $K_{ij}$  is the number of incoming connections to a neuron in population  $i$  from population  $j$ , and  $J_{ij}$  is the efficacy of a single synapse in the respective connection. Here,  $\circledast$  denotes element-wise multiplication, also called the Hadamard product (see Cichocki et al., 2009, for a consistent set of symbols for operations on matrices). Additionally, each neuron is driven by  $K_{\text{ext}}$  Poisson sources with rate  $\nu_{\text{ext}}$  and synaptic efficacy  $J_{\text{ext}}$ . All neurons in one population have identical parameters, so that we can describe the network activity in terms of population-averaged firing rates  $\nu_i$  due to population-dependent input  $\mu_i, \sigma_i$  determined by

the connectivity. Using the Fokker-Planck formalism, the stationary firing rates for each population  $i$  are given by (Fourcaud & Brunel, 2002)

$$\begin{aligned} \frac{1}{\nu_i} &= \tau_r + \tau_m \sqrt{\pi} \int_{\frac{\nu_r - \mu_i(\mathbf{A})}{\sigma_i(\mathbf{A})} + \gamma \sqrt{\frac{\tau_s}{\tau_m}}}^{\frac{\theta - \mu_i(\mathbf{A})}{\sigma_i(\mathbf{A})} + \gamma \sqrt{\frac{\tau_s}{\tau_m}}} e^{x^2} (1 + \operatorname{erf}(x)) dx \\ &=: 1/\Phi_i(\boldsymbol{\nu}, \mathbf{A}) \end{aligned} \quad (2)$$

$$\mu_i(\mathbf{A}) = \tau_m \sum_j K_{ij} J_{ij} \nu_j + \tau_m K_{\text{ext}} J_{\text{ext}} \nu_{\text{ext}} \quad (3)$$

$$\sigma_i^2(\mathbf{A}) = \tau_m \sum_j K_{ij} J_{ij}^2 \nu_j + \tau_m K_{\text{ext}} J_{\text{ext}}^2 \nu_{\text{ext}}, \quad (4)$$

which is correct up to linear order in  $\sqrt{\tau_s/\tau_m}$  and where  $\gamma = |\zeta(1/2)|/\sqrt{2}$ , with  $\zeta$  denoting the Riemann zeta function (Abramowitz & Stegun, 1974). Here,  $\mathbf{A}$  is chosen from the set of model parameters  $\{\mathbf{K}, \mathbf{J}, \nu_{\text{ext}}, \dots\}$ . If  $\mathbf{A}$  is a matrix, we vectorize it by concatenating its rows and indicate this by lower case, i.e.,  $\mathbf{a} = (a_{00}, a_{01}, \dots, a_{0N}, a_{10}, \dots, a_{1N}, a_{N0}, \dots, a_{NN}) = \operatorname{vec}(\mathbf{A}^T)^T$  following Magnus & Neudecker (1995). If the chosen parameter is a scalar we denote it with  $a$ . We find the fixed points of (2) by solving the first-order differential equation (Wong & Wang, 2006)

$$\dot{\boldsymbol{\nu}} := \frac{d\boldsymbol{\nu}}{ds} = \boldsymbol{\Phi}(\boldsymbol{\nu}, \mathbf{A}) - \boldsymbol{\nu}, \quad (5)$$

using the classical fourth-order Runge-Kutta method (RK4) with step size  $h = 0.01$  where  $s$  denotes a dimensionless pseudo-time. Note that (5) does not reflect the real time evolution of the population rates, but rather is a mathematical method to obtain the system's fixed points. In contrast to Wong & Wang (2006) we do not only search for stable fixed points, but also use (5) to obtain unstable attractors (cf. Results), an idea originating from the study of simple attractor networks by Amit & Brunel (1997b, esp. their Fig. 2 and Eq. 12).

The nonlinearity in the input-output relationship  $\boldsymbol{\Phi}$  in combination with feedback connections in general can cause multi-stability in the network. In particular excitatory-excitatory loops cause the system (5) to exhibit multi-stable behavior in the stationary firing rates. Thus we require a method to control the influence of these loops on the phase space of the network. As an illustration we first study the mechanism using the simple network architecture depicted in Fig. 2A: a population of excitatory neurons is coupled to itself with indegree  $K$  and is driven by external Poisson sources with the same indegree  $K_{\text{ext}} = K$  and rate  $\nu_{\text{ext}}$ . All connections have identical synaptic weights  $J$ . An increase in the external drive shifts the input-output relationship  $\boldsymbol{\Phi}(\boldsymbol{\nu}, a = \nu_{\text{ext}})$  of this one-dimensional system (Fig. 2C) to the left. The bifurcation diagram is shown in Fig. 2E: for low  $\nu_{\text{ext}}$  there is only one fixed point with low activity (LA). When increasing  $\nu_{\text{ext}}$ , a pair of fixed points of which one is stable and the other is unstable emerges via a saddle-node bifurcation, leading to a bistable system. The second stable fixed point exhibits high firing rates, denoted as the high-activity (HA) state. For even higher values of  $\nu_{\text{ext}}$ , the LA state loses stability.

In the bistable situation, the initial condition of (5) determines which fixed point the system settles in. However, studying the behavior for a particular initial condition is of minor interest, since the actual spiking network is a stochastic system which fluctuates around the fixed points of the deterministic system defined by (5). Even if we knew that (5) would relax to the LA fixed point for one particular initial condition, this would not necessarily imply that this state is indefinitely stable. Global stability is determined by the size of the basin of attraction of the LA fixed point. Suppose we want to increase the activity at the LA fixed point while maintaining its global stability. Adjusting the internal connectivity  $K$  to preserve the basin of attraction enables us to increase the external drive  $\nu_{\text{ext}}$ .

The equilibria given by the zeros of the velocity  $\dot{\nu}$  in the bistable case are shown in Fig. 2F. An increase of the drive on the one hand increases the firing rate of the LA fixed point (inset) but on the other hand reduces its basin of attraction, indicated by the colored bars in the top left corner. For illustrative purposes, we extend the problem to two dimensions by splitting the excitatory population into two subpopulations of equal size (Fig. 2B), mimicking a loop between excitatory populations in the model of macaque visual cortex (see Results). The corresponding (symmetric) two-dimensional phase space is shown in Fig. 2D. The basin of attraction for the LA fixed point, limited by the separatrix (Strogatz, 1994), is reduced for increased external drive. Since we have a bistable system, there must be at least one unstable fixed point on the separatrix at the intersection of the nullclines, i.e., the subspace for which the velocity  $\dot{\nu}_i$  in direction  $i$  vanishes. We use the unstable fixed point to control the basin of attraction. To this end, we study the behavior of the fixed points with respect to an infinitesimal change  $\delta\mathbf{a} = \mathbf{a}' - \mathbf{a}$  in the chosen model parameter. Let  $\nu^*(\mathbf{a})$  and  $\nu^*(\mathbf{a}')$  be the corresponding locations of the fixed points and  $\delta\nu^* = \nu^*(\mathbf{a}') - \nu^*(\mathbf{a})$  their separation. We can then expand  $\nu^*(\mathbf{a}')$  into a Taylor series up to first order in  $\delta\mathbf{a}$  and obtain

$$\begin{aligned}\nu^*(\mathbf{a}') &= \nu^*(\mathbf{a}) + \Delta_{\mathbf{a}}\delta\mathbf{a} \\ \Leftrightarrow \delta\nu^* &= \Delta_{\mathbf{a}}\delta\mathbf{a},\end{aligned}\tag{6}$$

with

$$\begin{aligned}\Delta_{\mathbf{a},ij} &= \frac{d\nu_i(\mu_i, \sigma_i)}{da_j} \\ &= \frac{d\Phi_i(\mu_i, \sigma_i)}{da_j} \\ &= \underbrace{\frac{\partial\Phi_i}{\partial\mu_i}}_{S_i} \frac{d\mu_i}{da_j} + \underbrace{\frac{\partial\Phi_i}{\partial\sigma_i} \frac{1}{2\sigma_i}}_{T_i} \frac{d\sigma_i^2}{da_j},\end{aligned}\tag{7}$$

where we notice that  $S_i$  and  $T_i$  only depend on the target population  $i$ . We accordingly define two diagonal matrices  $\mathbf{S}$  and  $\mathbf{T}$  with  $S_{ii} = S_i$  and  $T_{ii} = T_i$ . The derivatives with respect to  $a_j$  have the

compact expressions

$$\begin{aligned}\frac{d\mu_i}{da_j} &= \frac{\partial\mu_i}{\partial a_j} + \sum_n \frac{\partial\mu_i}{\partial\nu_n} \frac{d\nu_n}{da_j} \\ &= (\mathbf{D}_a\boldsymbol{\mu})_{ij} + \tau_m \sum_n \underbrace{(K_{in}J_{in})}_{=W_{in}} \Delta_{a,nj},\end{aligned}$$

with the Jacobian  $(\mathbf{D}_a\mathbf{f})_{ij} := \frac{\partial f_i}{\partial a_j}$  of some vector-valued function  $\mathbf{f}$  and

$$\frac{d\sigma_i^2}{da_j} = (\mathbf{D}_a\boldsymbol{\sigma}^2)_{ij} + \tau_m \sum_n \underbrace{(K_{in}J_{in}^2)}_{=W_{2,in}} \Delta_{a,nj},$$

where we use the Hadamard product again to define the matrix  $\mathbf{W}_2 := \mathbf{K} \circledast \mathbf{J} \circledast \mathbf{J}$ . Inserting the total derivatives into (7), we derive the final expression for  $\Delta_a$ , reading

$$\begin{aligned}\Delta_a &= S[\mathbf{D}_a\boldsymbol{\mu} + \tau_m \mathbf{W} \Delta_a] + T[\mathbf{D}_a\boldsymbol{\sigma}^2 + \tau_m \mathbf{W}_2 \Delta_a] \\ \Leftrightarrow \Delta_a &= \left[ \mathbb{1} - \underbrace{\tau_m(\mathbf{S}\mathbf{W} + \mathbf{T}\mathbf{W}_2)}_{=: \mathbf{M}} \right]^{-1} \underbrace{[\mathbf{S}\mathbf{D}_a\boldsymbol{\mu} + \mathbf{T}\mathbf{D}_a\boldsymbol{\sigma}^2]}_{=: \bar{\Delta}_a},\end{aligned}\quad (8)$$

where we use  $\mathbb{1}$  for the identity matrix and define the effective connectivity matrix  $\mathbf{M}$  and the matrix  $\bar{\Delta}_a$ . The latter has dimensionality  $N \times P$ , where  $P$  is the dimension of  $\mathbf{a}$  (for example,  $P = N^2$  for  $\mathbf{a} = \mathbf{k}$  the vector of indegrees). With the aid of (8), evaluating (6) at the unstable fixed point predicts the shift of the separatrix (Fig. 2D) to linear order. We now consider an additional parameter  $\mathbf{b}$  which is modified to counteract the shift of the unstable fixed point caused by the change in parameter  $\mathbf{a}$ , i.e.,

$$\begin{aligned}\Delta_a \delta a &\stackrel{!}{=} -\Delta_b \delta b \\ \Leftrightarrow \bar{\Delta}_a \delta a &= -\bar{\Delta}_b \delta b,\end{aligned}\quad (9)$$

where we used that the inverse of  $\mathbb{1} - \mathbf{M}$  appears on both sides of the equation and hence drops out. Note that  $(\mathbf{a}, \mathbf{b})$  represent any combination of model parameters, for example external input, indegrees, synaptic weights, etc. For a particular choice of  $(\mathbf{a}, \mathbf{b})$  we solve (9) for  $\delta\mathbf{b}$ . For the illustrative example shown in Fig. 2, where  $a = \nu_{\text{ext}}$  and  $b = K$ , (9) simplifies to

$$\delta K = \frac{\bar{\Delta}_{\nu_{\text{ext}}} \delta \nu_{\text{ext}}}{\Delta_K} = \frac{K_{\text{ext}} \delta \nu_{\text{ext}}}{\nu},$$

since  $S$  and  $T$  appearing in the respective  $\bar{\Delta}$ 's cancel each other. The resulting velocity of the system  $\Phi(a', b')$  ( $\Phi$  defines the system (5)) is shown in Fig. 2F. The firing rate in the LA fixed point is still increased as desired (inset), and the unstable fixed point coincides with that obtained in the original system  $\Phi(a, b)$ . This pattern of fixed points is also indicated by the zero vectors of the velocity field  $\dot{\nu}$  (Fig. 2D). The separatrix follows the unstable fixed point, and the basin of attraction in the system

$\Phi(a', b')$  is restored to that in the original system  $\Phi(a, b)$ . Fig. 2G shows the behavior of the LA fixed point in more detail. The modification of the parameter  $b$  does not noticeably change the location of the LA fixed point. In conclusion, the method allows us to increase the firing rates in the LA fixed point without modifying its basin of attraction.

To determine critical connections in a more complex model, we choose  $\mathbf{b} = \mathbf{k}$ , i.e. the vector of indegrees, and solve (9) with a decomposition into eigenmodes. We can write the right-hand side as

$$-(\bar{\Delta}_{\mathbf{k}} \delta \mathbf{k})_i = - \sum_j \tau_m (S_i J_{ij} + T_i J_{ij}^2) \nu_j \delta K_{ij}. \quad (10)$$

The equation holds because  $\mu_i, \sigma_i$  are only affected by connections to population  $i$ , and therefore their derivatives  $\partial \mu_i / \partial k_l, \partial \sigma_i / \partial k_l$  and hence  $\bar{\Delta}_{k,il}$ , vanish for  $l \notin [(i-1)N+1, iN]$ . We now make the ansatz

$$\delta K_{ij} = \sum_l \frac{\epsilon_l}{\tau_m} \frac{(\mathbf{u}^l \mathbf{v}^{lT})_{ij}}{(\mathbf{S}\mathbf{J} + \mathbf{T}(\mathbf{J} \circledast \mathbf{J}))_{ij}}, \quad (11)$$

which decomposes the changes  $\delta \mathbf{K}$  into eigenmodes of the effective connectivity. The  $\mathbf{u}^l$  and  $\mathbf{v}^l$  are the  $l$ -th right and left eigenvectors of  $\mathbf{M}$  as defined in (8), fulfilling the bi-orthogonality  $\mathbf{v}^{lT} \mathbf{u}^n = \delta_{ln}$  and the completeness relation  $\sum_l \mathbf{u}^l \mathbf{v}^{lT} = \mathbf{1}$ . Inserting (10) with (11) into (9) yields

$$\bar{\Delta}_{\mathbf{a}} \delta \mathbf{a} = - \sum_l \epsilon_l \mathbf{u}^l \mathbf{v}^{lT} \boldsymbol{\nu}. \quad (12)$$

Thus we can solve for  $\epsilon_l$  by multiplying from the left with  $\mathbf{v}^{nT}$

$$\begin{aligned} \underbrace{\mathbf{v}^{nT} \bar{\Delta}_{\mathbf{a}} \delta \mathbf{a}}_{=: \hat{a}^n} &= - \sum_l \epsilon_l \underbrace{\mathbf{v}^{nT} \mathbf{u}^l}_{\delta_{nl}} \underbrace{\mathbf{v}^{lT} \boldsymbol{\nu}}_{=: \hat{\nu}^l} \\ \epsilon_n &= - \frac{\hat{a}^n}{\hat{\nu}^n}. \end{aligned}$$

Our goal is to find a set of connections which dominate the size of the basin of attraction of the LA fixed point. Inserting (12) into (6) leads to

$$\begin{aligned} \delta \boldsymbol{\nu}^* &= \sum_l (\mathbf{1} - \mathbf{M})^{-1} \epsilon_l \mathbf{u}^l \mathbf{v}^{lT} \boldsymbol{\nu} \\ &= \sum_l \frac{\epsilon_l}{1 - \lambda_l} \mathbf{u}^l \hat{\nu}^l \\ &= \sum_l \frac{-\hat{a}^l}{1 - \lambda_l} \mathbf{u}^l, \end{aligned}$$

where  $\lambda_l$  are the eigenvalues of  $\mathbf{M}$ , which are either real or complex conjugate pairs since  $\mathbf{M} \in \mathbb{R}^{N \times N}$ . To determine the influence of each eigenmode on the shift of the fixed point, we project the eigenvectors

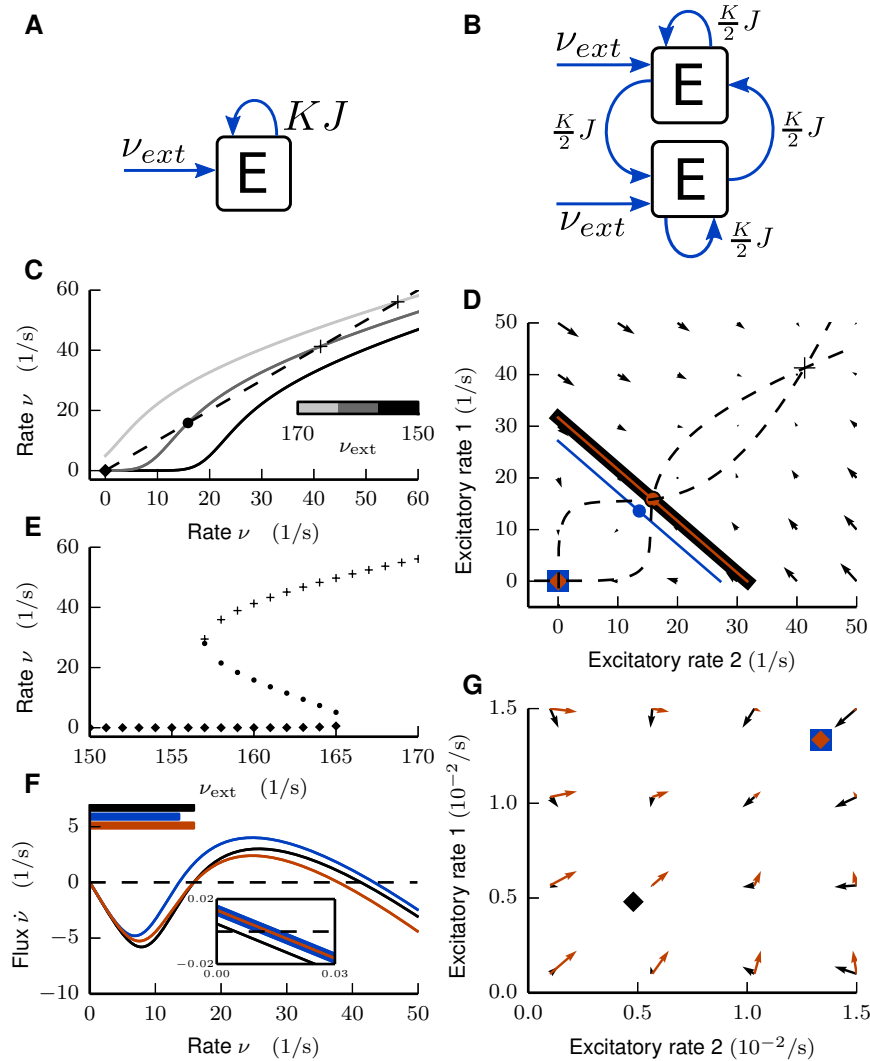


**Figure 2 Activity flow in an illustrative network example.** **Left column:** Global stability analysis in the single-population network. **A** Illustration of network architecture. **C** Input-output relationship  $\Phi(\nu, \nu_{\text{ext}})$  for different rates of the external Poisson drive  $\nu_{\text{ext}} = [150, 160, 170] \frac{1}{\text{s}}$  from black to light gray. Intersections with the identity line (dashed) mark fixed points of the system, which are shown in **E** as a function of  $\nu_{\text{ext}}$ . **F** Flux  $\dot{\nu}$  in the bistable case for  $\Phi(\nu_{\text{ext}} = 160 \frac{1}{\text{s}}, K)$  in black,  $\Phi(\nu'_{\text{ext}} = 161 \frac{1}{\text{s}}, K)$  in blue, and modified system  $\Phi(\nu'_{\text{ext}} = 161 \frac{1}{\text{s}}, K')$  in red. Intersections with zero (dashed line) mark fixed points. The inset shows an enlargement close to the LA fixed point. Horizontal bars at top of figure denote the size of the basin of attraction for each of the three settings. **Right column:** Global stability analysis in the network of two mutually coupled excitatory populations. **B** Illustration of network architecture. **D** Flow field and nullclines (dashed curves) for  $\Phi(\nu_{\text{ext}} = 160 \frac{1}{\text{s}}, K)$  and separatrices (solid lines), LA fixed point (rectangle), HA fixed point (cross) and unstable fixed points (circles) for  $\Phi(\nu_{\text{ext}} = 160 \frac{1}{\text{s}}, K)$  in black,  $\Phi(\nu_{\text{ext}} = 161 \frac{1}{\text{s}}, K)$  in blue, and  $\Phi(\nu_{\text{ext}} = 161 \frac{1}{\text{s}}, K')$  in red. The red separatrix and the red unstable fixed point coincide with the black ones. **G** Enlargement of D close to the LA fixed points.

$\mathbf{u}^l$  onto the fixed-point shift  $\delta\nu^*$  by multiplying each side with  $\delta\nu^* \delta\nu^{*\top}$  and solve again for  $\delta\nu^*$  to obtain

$$\delta\nu^* = \sum_l \frac{-\hat{a}^l}{1 - \lambda_l} \underbrace{\frac{\delta\nu^{*\top} \mathbf{u}^l}{\delta\nu^{*\top} \delta\nu^*}}_{=:\tilde{\eta}_l} \delta\nu^*, \quad (13)$$

where we define the (possibly complex-valued) coefficients  $\tilde{\eta}_l$ . We aim at a decomposition of  $\delta\nu^*$  into real components. If  $\text{Im}(\lambda_l) = 0$ ,  $\tilde{\eta}_l$  is real, so we can work directly with  $\eta_l := \tilde{\eta}_l$ . Complex eigenvalues  $\text{Im}(\lambda_l) \neq 0$  and corresponding eigenvectors come in conjugate pairs, so in this case we combine the corresponding coefficients  $\eta_l := \tilde{\eta}_l + \tilde{\eta}_l^*$ , to have all contributions  $\eta_l \in \mathbb{R}$  and  $\sum_l \eta_l = 1$  by construction (13). Each  $\eta_l$  quantifies how much of the total fixed-point shift can be attributed to the  $l$ -th eigenmode, which allows identification of the most effective eigendirection in the next section, where we apply the ansatz (11) to a multi-area, multi-layer model of macaque visual cortex.

The spiking simulations of the network model were carried out on the JUQUEEN supercomputer (Jülich Supercomputing Centre, 2015). All simulations were performed with NEST version 2.8.0 (Eppler et al., 2015) with optimizations for the use on the supercomputer which will be included in a future release. The simulations use a time step of 0.1 ms and exact integration for the subthreshold dynamics of the leaky integrate-and-fire neuron model (reviewed in Plesser & Diesmann, 2009).

## Results

We investigate a multi-scale network of cortical areas to understand the structural features essential for a realistic state of baseline activity. The model extends and adapts the microcircuit model of Potjans & Diesmann (2014), which covers 1 mm<sup>2</sup> surface area of early sensory cortex (Fig. 3A), to all vision-related areas of macaque cortex (Fig. 3B). Based on the microcircuit model, an area is composed of 4 layers (2/3, 4, 5, and 6) each having an excitatory (E) and an inhibitory (I) neural population, except parahippocampal area TH which consists of only 3 layers (2/3, 5, and 6). From anatomical studies, it is known that cortical areas in the macaque monkey are heterogeneous in their laminar structure and can be roughly categorized into 8 different architectural types based on cell densities and laminar thicknesses. This distinction was originally developed for prefrontal areas (Barbas & Rempel-Clower, 1997), and then extended to the entire cortex (Hilgetag et al., 2015). The visual cortex, and thus the model, comprises areas of categories 2, 4, 5, 6, 7 and 8. Precise layer-specific neuron densities are available for a number of areas, while for other areas, the neuron density is estimated based on their architectural type (see Schmidt et al. (2015a) for details).

The inter-areal connectivity is based on binary data from the CoCoMac database (Stephan et al., 2001; Bakker et al., 2012; Felleman & Van Essen, 1991; Rockland & Pandya, 1979; Barnes & Pandya, 1992) indicating the existence of connections, and quantitative data from Markov et al. (2014a). The latter are retrograde tracing data where connection strengths are quantified by the fraction of labeled neurons ( $FLN$ ) in each source area. The parcellation into different areas of our model follows the FV91

scheme proposed by Felleman & Van Essen (1991). The original analysis of the experimental data was performed in a different parcellation scheme, the M132 atlas of Markov et al. (2014a). Both parcellations have been registered to the F99 space (Van Essen, 2002), a standard macaque cortical surface included with the software tool Caret (Van Essen et al., 2001). This enables mapping between the two parcellations M132 and FV91.

On the target side, we use the exact coordinates of the injections to identify the equivalent area in the FV91 parcellation. To map the data on the source side from the M132 atlas to the FV91 parcellation, we count the number of overlapping triangles on the F99 surface between any given pair of regions and distribute data proportionally to the amount of overlap using the F99 region overlap tool on <http://cocomac.g-node.org>. In the model, this  $FLN$  is mapped to the indegree  $K_{AB}$  the target area  $A$  receives from source area  $B$  divided by its total indegree, i.e.,  $FLN_{AB} = K_{AB} / \sum_{B'} K_{AB'}$ . Here,  $K_{AB}$  is defined as the total number of synapses between  $A$  and  $B$  divided by the total number of neurons in  $A$ . On the source side, laminar connection patterns are based on CoCoMac (Felleman & Van Essen, 1991; Barnes & Pandya, 1992; Suzuki & Amaral, 1994; Morel & Bullier, 1990; Perkel et al., 1986; Seltzer & Pandya, 1994) and on fractions of labeled neurons in the supragranular layers ( $SLN$ , Markov et al., 2014b). Gaps in these data are bridged exploiting a sigmoidal relation between  $SLN$  and the logarithmized ratio of overall cell densities of the two areas. We map the  $SLN$  to the ratio between the number of synapses originating in layer 2/3 and the total number of synapses between the two areas, assuming that only excitatory populations send inter-area connections, i.e.,  $SLN_{AB} = \sum_i K_{AB}^{i,2/3E} N_A^i / \sum_{i,j} K_{AB}^{ij} N_A^i$ , where the indices  $i$  and  $j$  go over the different populations within area  $A$  and  $B$ , respectively. In the context of the model, we use the terms  $FLN$  and  $SLN$  to refer to the relevant relative indegrees given here. On the target side, the CoCoMac database provides data from anterograde tracing studies (Felleman & Van Essen, 1991; Rockland & Pandya, 1979; Jones et al., 1978; Seltzer & Pandya, 1991). A detailed description of the data integration is given in Schmidt et al. (2015a).

Simulations of the model (Fig. 3C) reveal that, though realistic levels of activity can be achieved for populations in layers 2/3 and 4, populations 5E and 6E of the majority of areas show vanishingly low or zero activity in contrast to empirical data (Swadlow, 1988; de Kock & Sakmann, 2009). Missing inputs in the model, i.e., from subcortical and non-visual cortical areas, are replaced by Poissonian spike trains, whose rate  $\nu_{\text{ext}}$  is a free, global parameter. In the original model all populations of a particular area receive the same indegree of external inputs  $K_{\text{ext}}$ . The only exception to this rule is area TH where the absence of granular layer 4 is compensated by an increase of the external input to populations 2/3E and 5E by 20%. To elevate the firing rates in the excitatory populations in layers 5 and 6, we enhance the external Poisson drive, parametrized by the  $K_{5E,\text{ext}}$  incoming connections per target neuron (indegree), of the 5E population by increasing  $\kappa = K_{5E,\text{ext}} / K_{\text{ext}}$ . The simultaneous increase in the drive of 6E needs to be stronger, since the firing rates in population 6E of the original model (Fig. 3C) are even lower than the rates of 5E (averaged across areas: 0.09 spikes/s for 5E compared to  $2 \cdot 10^{-5}$  spikes/s for 6E). We thus scale up  $K_{6E,\text{ext}}$  linearly with  $\kappa$  such that  $\kappa = 1.15$  results in  $K_{6E,\text{ext}} / K_{\text{ext}} = 1.5$ . However,

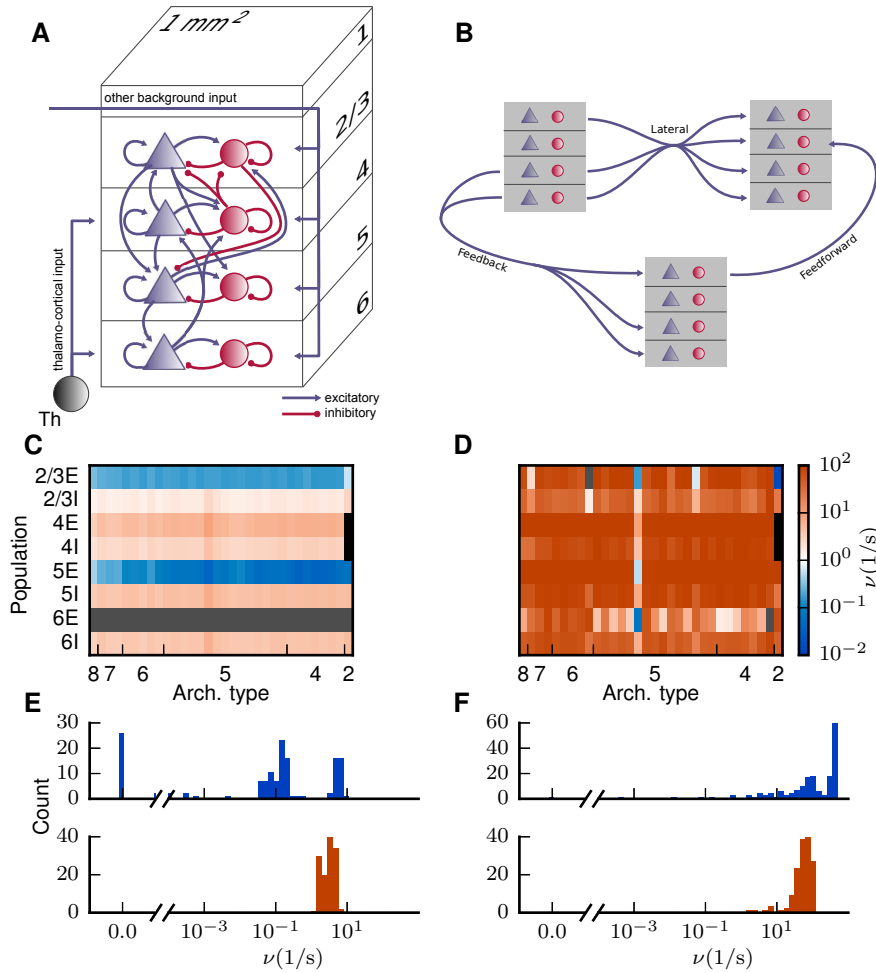


**Figure 3 Bistability of the model.** **A** Sketch of the microcircuit model serving as a prototype for the areas of the multi-area model (adapted from Potjans & Diesmann, 2014, with permission). **B** Sketch of the most common laminar patterns of cortico-cortical connectivity of the multi-area model. **C** Population-averaged firing rates encoded in color for a spiking network simulation of the multi-area model with low external drive ( $\kappa = 1.0$ ). **D** As **C** but for increased external drive ( $\kappa = 1.125$ ). The color bar refers to both panels. Areas are ordered according to their architectural type along the horizontal axis from V1 (type 8) to TH (type 2) and populations are stacked along the vertical axis. The two missing populations 4E and 4I of area TH are marked in black and firing rates  $< 10^{-2}$  Hz in gray. **E** Histogram of population-averaged firing rates shown in **C** for excitatory (red) and inhibitory (blue) populations. The horizontal axis is split into linear- (left) and log-scaled (right) ranges. **F** as **E** corresponding to state shown in **D**.

already a perturbation of a few percent leads to a state with unrealistically high rates (Fig. 3D), caused by the reduced basin of attraction of the low-activity state similar to Fig. 2D. Our aim now is to improve the working point of the model such that all populations exhibit spiking activity  $\geq 0.05$  spikes/s while preventing the model from entering a state of unrealistically high rates of  $\geq 30$  spikes/s (Swadlow, 1988; de Kock & Sakmann, 2009). The employed technique exposes the mechanism giving rise to the observed instability and identifies the circuitry responsible for this dynamical feature.

In the following we choose the inactive state  $\nu(0) = (0, \dots, 0)^T$  as the initial condition. The exact choice is not essential since we are only interested in the fixed points of the system. Fig. 4B shows the integration of (5) over pseudo-time  $s$  for different increased levels of the external drive to populations 5E and 6E parametrized by  $\kappa$ . For low values of  $\kappa$ , the integration converges to the LA fixed point shown in

Fig. 4D, and is in agreement with the activity emerging in the simulation (Fig. 3C). For increased values of  $\kappa$ , the system settles in the HA fixed point (Fig. 4E), again in agreement with the simulation. The population-specific firing rates in the HA state found in the mean-field predictions (Fig. 4E) are also close to those in the simulation (Fig. 3D), but minor deviations occur due to the violation of the assumptions made in the diffusion approximation. In particular, at these pathologically high rates, the neurons fire regularly and close to the reciprocal of their refractory period, while in the mean-field theory we assume Poisson spike statistics. Still, the mean-field theory predicts the bistability found in the simulation. Since the theory yields reliable predictions in both stable fixed points, we assume that also the location of the unstable fixed point in between these two extremes is accurately predicted by the theory.

To stabilize the LA fixed point for increased values of the external drive  $\kappa$ , we apply the procedure derived in Materials and Methods. To this end we need to find the unstable fixed point of the system. This is nontrivial since the high-dimensional system of equations (2) is not directly solvable for the fixed-point firing rates, and the numerical integration of (5) for finding equilibria by construction only converges to stable fixed points. If the unstable fixed point has only one repelling direction (Fig. 6A), it constitutes a stable attractor on the  $N - 1$  dimensional separatrix. The separatrix is a stable manifold (Strogatz, 1994), and therefore a trajectory originating in its vicinity but not near an unstable fixed point initially stays in the neighborhood. If an initial condition just outside the separatrix is close to the basin of attraction of a particular unstable fixed point, the trajectory initially approaches the latter. Close to the fixed point the velocity is small. Ultimately trajectories diverge from the separatrix in the fixed point's unstable direction, as illustrated in Fig. 4A. In conclusion, we expect a local minimum in the velocity along the trajectories close to the unstable fixed point. To estimate the location of the unstable fixed point in this manner, we need to find initial conditions close to the separatrix. Naively, we would just fix the value of  $\kappa$  and vary the initial condition. However, due to the high dimensionality of our system, this is not feasible in practice, and we vary  $\kappa$  for a fixed initial condition instead (Fig. 4B). Fig. 4B shows the firing rate averaged across populations for two trajectories starting close to the separatrix, where the first one converges to the LA fixed point and the second one to the HA state. The trajectories diverge near the unstable fixed point and thus we define the last local minimum of the Euclidean norm of the velocity vector as the critical time  $s_c$  at which we assume the system to be close to the unstable fixed point (Fig. 4C). We find four relevant and distinct unstable fixed points, of which two are shown in Fig. 5.

To counteract the shift of the separatrix caused by the increase in  $\kappa$ , we follow the procedure described in Materials and Methods. We subject the modifications of connectivity following from the application of the method to the following constraints. In line with the anatomical literature, we do not allow for changes of the connectivity that would lead to cortico-cortical connections originating in the granular layer 4 (Felleman & Van Essen, 1991), and we also disallow inhibitory cortico-cortical connections, as the vast majority of long-range connections are known to be excitatory (Salin & Bullier, 1995; Tomioka & Rockland, 2007). In addition, we naturally restrict indegrees to positive values. We find that four iterations (numbered by index  $j$ ) corresponding to the four distinct unstable fixed points suffice to preserve

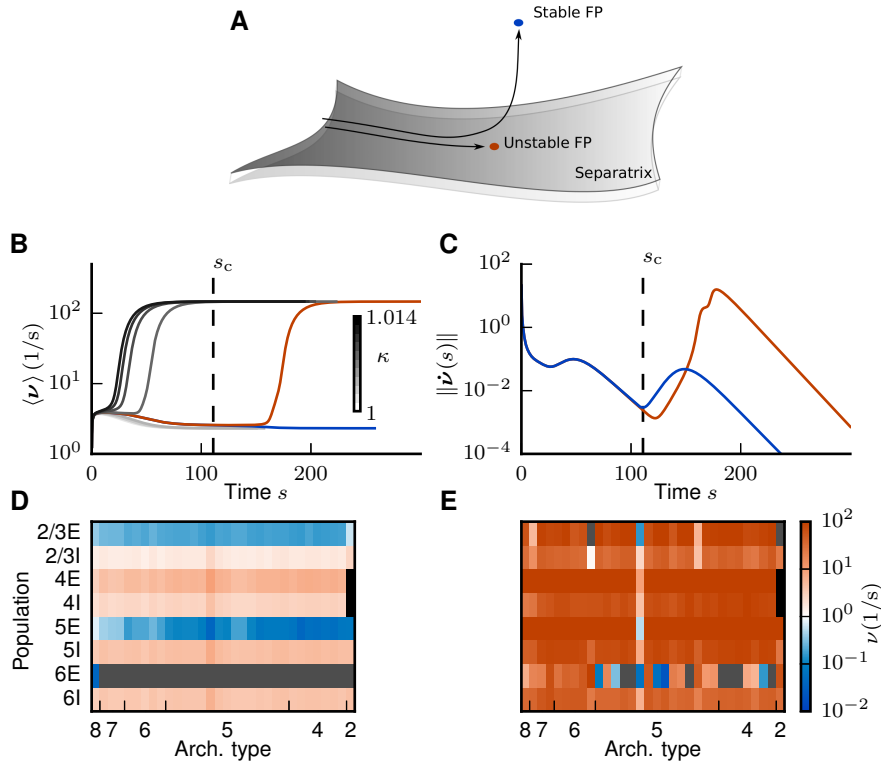


**Figure 4 Application of the mean-field theory to the multi-area model of visual cortex.** **A** Trajectories starting inside the separatrix converge to an unstable fixed point. Trajectories starting close to the separatrix are initially attracted by the unstable fixed point but then repelled in the fixed point's unstable direction and finally converge to a stable fixed point. **B** Firing rate averaged across populations over time. Integration of (5) leads to convergence to either the low-activity (LA) or the high-activity (HA) attractor for different choices of the external input factor  $\kappa$ . We show eight curves with  $\kappa$  varying from 1.0 to 1.014 in steps of 0.002 and two additional curves for  $\kappa = 1.007662217$ ,  $1.007662218$ . The curves for the largest factor ( $\kappa = 1.007662217$ ) that still leads to the LA state and for the smallest factor ( $\kappa = 1.007662218$ ) that leads to the HA state are marked in blue and red, respectively. The four curves with  $\kappa \leq 1.006$  coincide with the blue curve. **C** Euclidean norm of the velocity vector in the integration of (5) for the different choices of  $\kappa$ . The vertical dashed line indicates the time  $s_c$  of the last local minimum in the blue curve. **D** Stationary firing rate in the different areas and layers of the model in a low-activity state for  $\kappa = 1.0$  as predicted by the mean-field theory (same display as in Fig. 3). **E** As **D**, but showing the high-activity state for  $\kappa = 1.125$ .

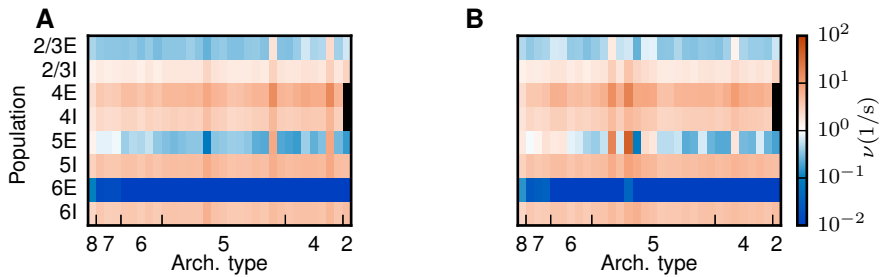


**Figure 5 Unstable fixed points in subsequent iterations.** Population firing rates at the unstable fixed point as predicted by the mean-field theory encoded in color for iterations 1 (**A**) and 2 (**B**). Same display as in Fig. 3.

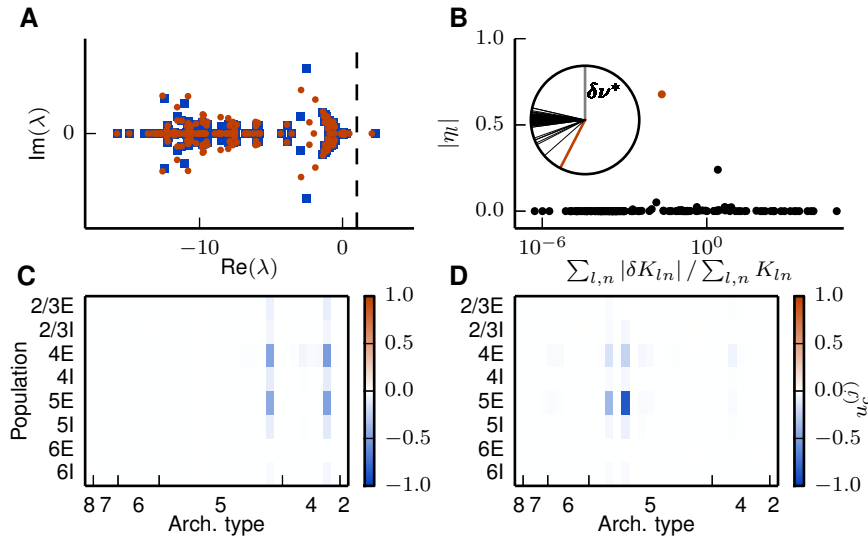


**Figure 6 Eigenspectrum analysis of network stability.** **A** Eigenvalue spectrum of the effective connectivity matrix  $M$  for the first (blue squares) and second (red dots) iteration. The dashed vertical line marks the edge of stability at a real part of 1. **B** Contribution  $\eta_l$  of an individual eigenprojection  $l$  to the shift of the unstable fixed point (13) versus the relative change in indegrees associated with  $l$  for the first iteration. The data point corresponding to  $\lambda_c^{(1)}$  is marked in red. The inset shows the relative angles between  $\delta\nu^*$  and the eigenvectors  $u^l$ . The red line corresponds to the critical eigendirection. **C** Entries of the eigenvector  $u_c^{(1)}$  associated with  $\lambda_c^{(1)}$  in the populations of the model. The affected areas are 46 and FEF. **D** Same as **C** for the second iteration.

the basin of attraction of the LA state with respect to an increase of the external drive up to  $\kappa = 1.15$ . In the following we concentrate on iterations 1 and 2, where the second one is also representative for iterations 3 and 4, which are qualitatively alike. In each iteration  $j$  there is exactly one unstable eigendirection with an eigenvalue  $\text{Re}(\lambda_c^{(j)}) > 1$  (Fig. 6A). The associated critical eigenvector is approximately anti-parallel to the shift of the fixed point,  $\delta\nu^*$  (inset of Fig. 6B), and of similar length. The critical eigendirection (red dot in Fig. 6B) constitutes the most effective modification, giving the largest contribution to the desired shift while requiring only a small change of 2.3% in average total indegrees.

The associated eigenvector  $u_c^{(1)}$  predominately points into the direction of populations 4E and 5E of areas FEF and 46 (Fig. 6C), while  $u_c^{(2)}$  has large entries in the 5E populations of two areas (Fig. 6D). The high rates of these populations at the unstable fixed points (cf. Fig. 5A,B with Fig. 6C,D) reflect that the instability is caused by increased rates in excitatory populations. Considering the other iterations (not shown) as well, these instabilities occur particularly in population 5E. Each iteration shifts the transition to the HA state (the value of  $\kappa$  for which the separatrix crosses the initial condition) to higher values of  $\kappa$  and increases the attainable rates of populations 5E and 6E in the LA state (Fig. 7A). After all four iterations, the average total indegrees (summed over source populations) of the system are changed by 11.3%. The first iteration mainly affects connections within and between areas 46 and FEF (Fig. 7B). In particular, the excitatory loops between the two areas are reduced in strength, especially those involving layer 5 (Fig. 7C). We thus identify two areas forming a critical loop. In the second iteration, the changes are spread across areas (Fig. 7D). In conclusion, the method identifies critical structures in the model both on the level of areas and on the level of layers and populations, and leads to a small but specific

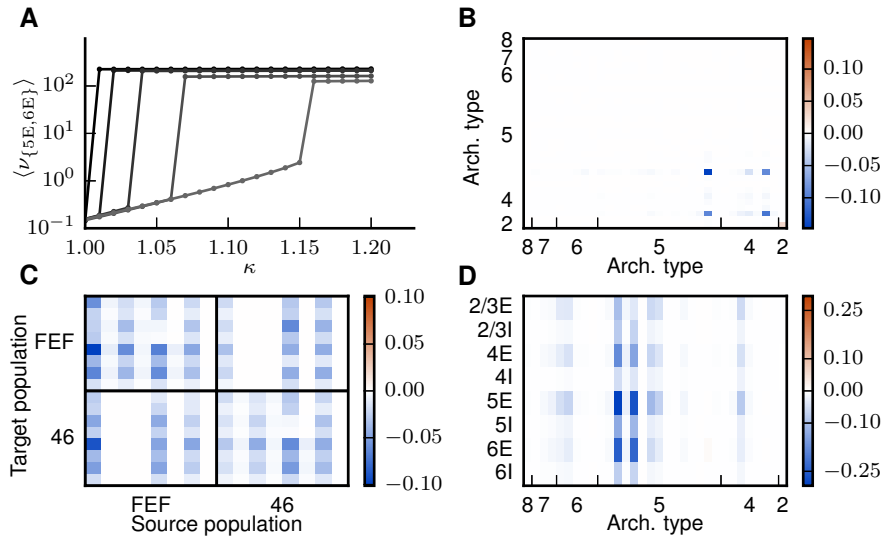


**Figure 7 Altered phase space and modified connections.** **A** Firing rates averaged across populations 5E and 6E and across areas for different stages from the original model (black) to iteration 4 (light gray) as a function of  $\kappa$ , predicted by the mean-field theory. **B** Relative changes in the indegree  $\delta K_{AB} / \sum_B K_{AB}$  between areas  $A, B$  in the first iteration. **C** Layer-specific relative changes  $\delta K_{ln} / \sum_n K_{ln}$  in the connections within and between areas FEF and 46, for the first iteration. Populations are ordered from 2/3E (left) to 6I (right) on the horizontal axis and from 6I (bottom) to 2/3E (top) on the vertical axis as in panel **D**. **D** Relative changes in population-specific indegrees summed over source populations,  $\sum_n \delta K_{ln} / \sum_n K_{ln}$ , for the second iteration.

structural change of the model.

In the following we analyze the modifications of the connectivity with respect to the internal and inter-area connections in detail. The intrinsic circuits of the areas are modified in different directions, as shown for two exemplary areas V4 and CITv in Fig. 8A. Despite this heterogeneity, significant changes affect mostly excitatory-excitatory connections (Fig. 8A) with connections to population 5E experiencing the most significant changes (Fig. 7B,D). In fact, the anatomical data (Binzegger et al., 2004) underlying the microcircuit model (Potjans & Diesmann, 2014) contain only two reconstructed excitatory cells from layer 5, but considerably more for other cell types, indicating a higher uncertainty for layer 5 connections. Fig. 8B shows the correlation between intrinsic connectivity changes for all pairs of areas, with areas ordered according to a hierarchical clustering using a farthest point algorithm (Voorhees, 1986) on the correlation matrix. We find 4 clusters each indicating a group of areas which undergo changes with similar patterns. The groups are displayed in different colors in the histogram in Fig. 8B. Areas with architectural type 4, 5 and 6 are distributed over several clusters. We can interpret this as a differentiation of these types into further subtypes. The resulting changes of the intra-areal connectivity are small (Fig. 8A), but still significant for network stability.

Connections between areas can be characterized by their *FLN* and *SLN*. The *FLN* reflects the overall strength of an inter-areal connection and is only weakly affected across connections (Fig. 8C), with a correlation between original and modified logarithms of *FLN* of  $r_{\text{Pearson}} = 0.79$ . Significant variations in the *FLN* occur mostly for very weak connections where the relative uncertainties in the experimental data are likely to be substantial. The two overlapping red dots in Fig. 8C represent the

connections between areas 46 and FEF, which are modified in the first iteration (cf. Fig. 7C). The *SLN* determines the laminar pattern of the location of source neurons for cortico-cortical connections. Overall, data are available for 24% of the inter-areal connections in the parcellation of Felleman & Van Essen (1991), while the *SLN* for the rest are derived from the sigmoidal law. The majority of connections undergo small changes in their laminar source pattern (Fig. 8D) and connections with large modifications ( $|\delta SLN| > 0.5$ ) are weak (average  $\overline{FLN} = 6 \cdot 10^{-4}$  compared to  $\overline{FLN} = 10^{-2}$  in the model as a whole). Because weak connections are represented by low neuron counts, they have a relatively large uncertainty in their laminar patterns, justifying larger adjustments. Spearman's rank correlation between the *SLN* of the original model that were directly taken from experiments and the logarithmized ratios of cell densities is  $\rho = -0.63$  ( $p = 3 \cdot 10^{-11}$ , p-value of a two-sided test for uncorrelated data). For the modified model, we take the *SLN* of all connections into account and obtain  $\rho = -0.40$  ( $p = 6 \cdot 10^{-20}$ ), indicating a reduced, but still significant, monotonic dependence between *SLN* and the logarithmized ratios of cell densities.

To judge the size of the modification to the connectivity, we compare it to the variability of measured cortico-cortical connection densities (Markov et al., 2014a). We quantify the latter as the average inter-individual standard deviation of the logarithmic *FLN*, i.e.,  $\sigma = \left\langle \sqrt{(\log FLN - \overline{\log FLN})^2} \right\rangle$ , where the overbar  $\overline{\cdot}$  denotes the average over injections and  $\langle \cdot \rangle$  the average over connections. This variability equals 2.17 while the average modification of the logarithmic *FLN* is 1.34. The main experimental connection probabilities used to construct the intra-areal connectivity of the model have an average relative standard deviation of 30% across electrophysiological experiments (cf. Table 1 of Potjans & Diesmann, 2014) while the intra-areal connection probabilities of the model are modified by 9% on average. Scannell et al. (2000) report even greater variability in a review on cortico-cortical and thalamocortical connectivity. These considerations show that the changes applied to the connectivity are well within the uncertainties of the data. Overall, 35 out of 603 connections were removed from the network. In the CoCoMac database, 83% of these are indicated by only a single tracer injection, while the overall proportion of connections measured by a single injection is 59%.

We simulated the full spiking network model with the modified connectivity matrix and  $\kappa = 1.125$  to avoid being too close to the transition (7A). This results in reasonable rates across populations and areas (Fig. 9B, D). The average rates in populations 5E and 6E are increased compared to a simulation of the original model from 0.09 and  $2 \cdot 10^{-5}$  spikes/s to 3.0 and 0.4 spikes/s, respectively. All populations exhibit firing rates within a reasonable range between 0.05 and 30 spikes/s (Fig. 9D), as opposed to the original state in which a considerable fraction of excitatory neurons was silent (Fig. 3E). The theoretical prediction is generally in agreement with the rates obtained in the simulation (Fig. 9A, C). Discrepancies are caused by violations of the employed assumptions, i.e., Poissonian spiking statistics (Fourcaud & Brunel, 2002). Moreover, we observe broad distributions of firing rates over neurons in the simulated data, seemingly in conflict with the reduction to population-averaged firing rates used by our framework. Nevertheless, the differences between theory and simulation are small, and negligible for the central aim of the study: the integration of activity constraints into the data-driven construction of multi-scale neuronal networks.

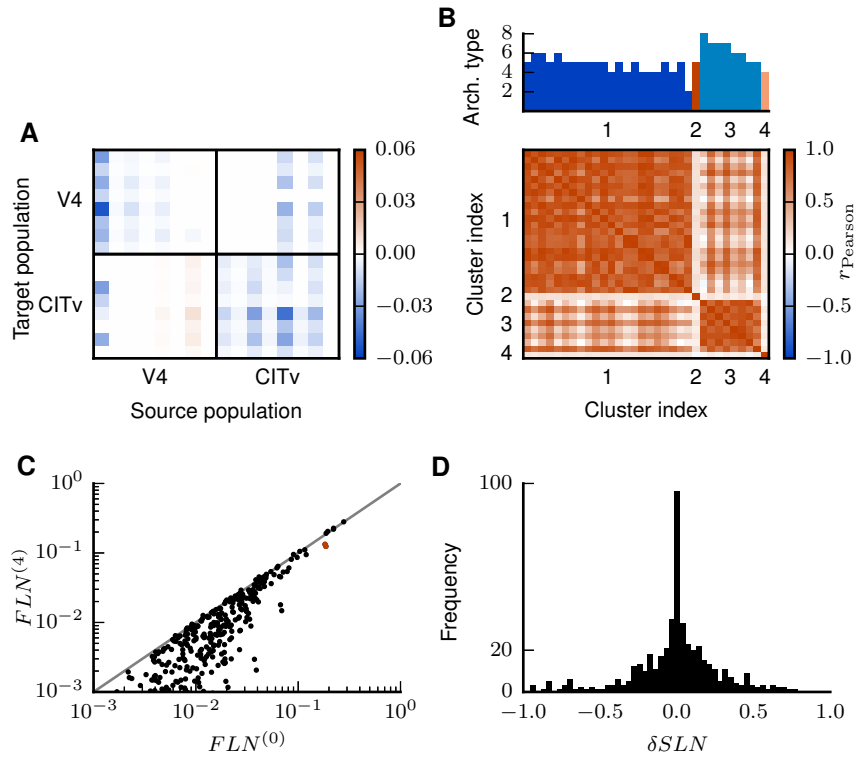


**Figure 8 Analysis of changes in connectivity.** **A** Changes in the indegrees within and between exemplary areas V4 and CITv relative to the total indegrees of the target populations, i.e.,  $\delta K_{ln} / \sum_n K_{ln}$ . Populations ordered as in Fig. 7C. **B** Pearson correlation coefficient of the changes of the internal indegrees  $\delta K_{AA}^{ij}$  between all pairs of the 32 areas. Areas ordered according to hierarchical clustering using a farthest point algorithm (Voorhees, 1986). The heights of the bars on top of the matrix indicate the architectural types of the areas (types 1 and 3 do not appear in the model) with color representing the respective clusters. **C**  $FLN$  of the modified connectivity after 4 iterations versus the original  $FLN$  of the model. Only  $FLN > 10^{-3}$  are shown for a better overview. The overlapping red dots represent the connections between areas 46 and FEF. Unity line shown in gray. **D** Histogram of the changes in  $SLN$  ( $\delta SLN = SLN^{(4)} - SLN^{(0)}$ ).

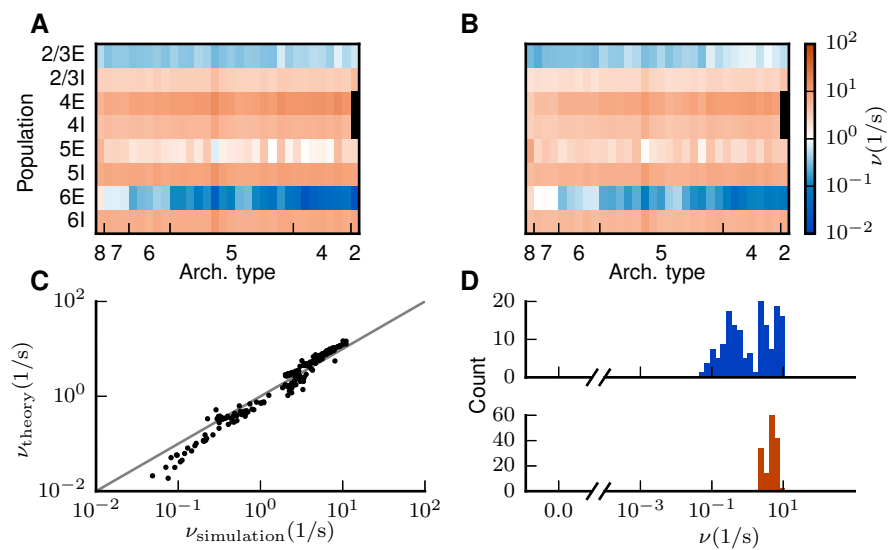


**Figure 9 Improved low-activity fixed point of the model.** Population-averaged firing rates for  $\kappa = 1.125$  encoded in color (**A**) predicted by the analytical theory and (**B**) obtained from the full simulation of the spiking network. Same display as in Fig. 3. **C** Analytical versus simulated firing rates (black dots) and identity line (gray). **D** Histogram of population-averaged simulated firing rates. Same display as in Fig. 3.

## Discussion

This study investigates the link between experimentally measured structural connectivity and neuronal activity in a multi-scale spiking network model of macaque visual cortex (Schmidt et al., 2015a). We devise a theoretical method that systematically combines anatomical connectivity with physiological activity constraints. Already weak constraints requiring the activity to neither vanish nor be pathologically high yield a set of specific but minimal structural modifications for increasing the model’s excitation to a realistic level. The procedure constrains the experimentally obtained connectivity maps to a realization that is compatible with physiological experiments. This establishes a path from experimentally observed activity to specific hypotheses about the anatomy and demands for further experiments.

Connections are modified both inside and between cortical areas, on average well within the known uncertainties of the underlying data. The model areas are based on the early sensory cortex model of Potjans & Diesmann (2014). This circuit is adapted to individual areas by taking into account neuronal densities and laminar thicknesses. The model definition renders areas with equal architectural type similar in their internal connectivity, a drastic but inevitable simplification due to the lack of more detailed experimental data. The proposed method softens this assumption: small adaptations of internal connectivity distinguish the architectural types into further subtypes. These modifications are significant for the global stability of the network. Thus, our approach enables purely anatomy-based area categorizations to be refined with dynamical information.

Connections between areas are changed in terms of total strength and laminar patterns. Overall, the changes are small, but significant for specific connections. The loop formed by areas 46 and FEF is critical to the global stability of the network. Both areas have been investigated by Markov et al. (2014a), albeit in a different parcellation scheme than the Felleman & Van Essen (1991) scheme used here. Our method suggests a weaker coupling of these two areas than found in the anatomical data set. Uncertainties, partly due to the mapping between parcellations, leave room for this interpretation. Areas 46 and FEF belong to prefrontal cortex and are multimodal, indicating that the influence of other parts of cortex could stabilize them, a mechanism outside the scope of the present visual cortex model. Both explanations can be tested either in an experimental study or with an extended model.

A few weak connections undergo large changes in their laminar patterns. With the present activity constraints, the method hereby weakens hierarchical relations in the model structure, indicating that preserving these relations requires additional dynamical constraints such as layer-specific coherence between areas (van Kerkoerle et al., 2014; Bastos et al., 2015). Conversely, it is possible to achieve satisfactory population rates with a less pronounced hierarchical structure.

Our analysis reveals that layer 5 excitatory cells play a critical role in the model’s dynamics, in line with the observed ongoing dynamics in mammalian neocortex (Sanchez-Vives & McCormick, 2000; Beltramo et al., 2013). This critical role is often attributed to single-neuron properties, with a subset of layer 5 neurons displaying pacemaker activity (Le Bon-Jego & Yuste, 2007; Lorincz et al., 2015; Neske

et al., 2015). We find that the network architecture itself already explains a strong impact of layer 5 on the phase space of the network suggesting that single-neuron properties and network structure jointly enable layer 5 to exert its dominant influence.

The cortico-cortical connectivity of the model is compiled from the extensive dataset of Markov et al. (2014a) combined with the CoCoMac database (Stephan et al., 2001; Bakker et al., 2012), which collects data from hundreds of tracing studies. One could consider alternative methods for combining this information into one connectivity graph, for instance taking into account how consistently a given connection is reported across studies (Schmitt et al., 2014), and compare different methods by analyzing the resulting network dynamics. The presented mean-field theory could then be used to estimate the firing rates of each network instance without performing time-consuming simulations. However, here we first choose the integrative approach that accumulates all available experimental evidence into a single model and afterwards modify the resulting connectivity with our analytical procedure, thereby effectively sorting out uncertain connections.

The theory uses the diffusion approximation to derive a self-consistency equation for the stationary population rates valid for high indegrees and small synaptic efficacies. These requirements are fulfilled in the multi-area model and therefore the theoretical prediction agrees with the stationary activity of the simulation. Moreover, the theory predicts the bistability of the model, which is non-trivial, as the mean-field assumption of Poisson statistics of the activity is generally violated in the high-activity state. Nevertheless, since the activity in this state is mostly driven by strong mean inputs and the theory converges to the noiseless solution in the mean-driven limit, its predictions still provide a viable approximation. The firing rates in the unstable fixed points are predominantly low, while the exceptions with very high rates are again mean-dominated. Presumably the theory therefore predicts the locations of these fixed points and consequently the global stability properties with sufficient accuracy. To preserve the global stability of the system, we keep the position of the separatrix invariant, which we approximately achieve by preserving the location of unstable fixed points on the separatrix. To this end, we use a linearization around these locations and an eigenmode decomposition to identify the set of connections to adjust. In the multi-area model, this linearization is justified because the system operates close to an instability so that only minor modifications are required. The method can be generalized to larger modifications by changing parameters iteratively in small steps.

In this study we restrict ourselves to leaky integrate-and-fire model neurons, consistent with the key concept of the models we consider: individual cells are modeled in a simple manner to expose the impact of structural connectivity on the network dynamics. Moreover, the current-based leaky integrate-and-fire neuron can reproduce in-vivo like activity (Rauch et al., 2003; Jolivet et al., 2006) and is analytically tractable, which enables the identification of mechanisms underlying specific network effects. More complex neuron models can be incorporated into the theory by replacing the gain function of each neuronal population with an analytical expression or an interpolated function obtained from spiking single-neuron simulations. For example, one could use a conductance-based point-neuron model, featuring a non-

monotonic gain function: the gain is reduced if excitatory and inhibitory inputs are increased in a balanced manner (Kuhn et al., 2004). Generally, this renders a system more stable. However, the bistability considered in our work is caused by excitatory inputs. Since conductance-based models also show a monotonically increasing gain function in dependence of the excitatory conductance alone, we expect the bistability to occur for such models as well.

Biological networks have various stabilization mechanisms not considered here, which render them less critical. For instance, during growth, homeostatic mechanisms guide the system toward the right structure. Furthermore, short-term synaptic plasticity (reviewed in Morrison et al., 2008), homeostatic synaptic scaling (Turrigiano et al., 1998) and spike-frequency adaptation (e.g. summarized in Benda & Herz, 2003) may prevent the system from entering the high-activity state. However, introducing these self-organizing mechanisms increases model complexity, causing a more intricate relation between structure and activity. Therefore, we start from a mean-field description on the level of neuronal populations, ignoring details of synaptic dynamics. Mild constraints on the activity lead to a network structure within the anatomical range of parameters. This network yields globally stable activity, suggesting that additional stabilization mechanisms are not required to achieve this.

The observed inter-individual variability may reflect that mechanisms of self-organization and homeostasis find structurally different implementations of the same function. Thus, in studies across individuals we cannot expect progress in experimental technology to narrow down the variability of parameters indefinitely. The combined ranges of parameters rather specify the solution space, and our method provides a way to find a particular solution.

In principle, the method applies to any model parameter. It would be possible to modify, for example, synaptic weights. Since experimental data on synaptic weights are sparse, this is another natural choice. Moreover, such an analysis may provide hints about suitable synaptic plasticity rules that dynamically stabilize the model.

Experimental data on stationary activity in cortex are sparse. We therefore restrict ourselves to fundamental constraints and increase the drive to the model in an area-unspecific way to fulfill them. The resulting heterogeneity of the firing rates across areas is thus not imposed by the method, but rather arises from the connectivity that remains strongly informed by anatomical data. Alternatively, one could predefine a desired state and investigate the parameter changes necessary to achieve it.

In the present work, the analytical combination of anatomy and activity data into a consistent model is restricted to stationary firing rates. In future studies, also higher-order statistical measures of activity can be used as constraints. Resting-state fMRI, for example, provides information on the functional connectivity between areas as a second-order measure. When combined with analytical predictions of functional connectivity, the method may shed light on the anatomical connection patterns underlying inter-area communication.

## References

- Abramowitz, M & Stegun, IA (1974). *Handbook of Mathematical Functions: with Formulas, Graphs, and Mathematical Tables*. (New York: Dover Publications).
- Amit, DJ & Brunel, N (1997a). Dynamics of a recurrent network of spiking neurons before and following learning. *Network: Comput Neural Systems* 8:373–404.
- Amit, DJ & Brunel, N (1997b). Model of global spontaneous activity and local structured activity during delay periods in the cerebral cortex. *Cereb Cortex* 7:237–252.
- Axer, M, Grässel, D, Kleiner, M, Dammers, J, Dickscheid, T, Reckfort, J, Hütz, T, Eiben, B, Pietrzyk, U, Zilles, K, et al. (2011). High-resolution fiber tract reconstruction in the human brain by means of three-dimensional polarized light imaging. *Front Neuroinformatics* 5.
- Bakker, R, Thomas, W, & Diesmann, M (2012). CoCoMac 2.0 and the future of tract-tracing databases. *Front Neuroinformatics* 6.
- Barbas, H & Rempel-Clower, N (1997). Cortical structure predicts the pattern of corticocortical connections. *Cereb Cortex* 7:635–646.
- Barnes, CL & Pandya, DN (1992). Efferent cortical connections of multimodal cortex of the superior temporal sulcus in the rhesus monkey. *J Compar Neurol* 318:222–244.
- Bastos, AM, Vezoli, J, Bosman, CA, Schoffelen, JM, Oostenveld, R, Dowdall, JR, De Weerd, P, Kennedy, H, & Fries, P (2015). Visual areas exert feedforward and feedback influences through distinct frequency channels. *Neuron* 85:390–401.
- Beltramo, R, D’Urso, G, Maschio, MD, Farisello, P, Bovetti, S, Clovis, Y, Lassi, G, Tucci, V, Tonelli, DDP, & Fellin, T (2013). Layer-specific excitatory circuits differentially control recurrent network dynamics in the neocortex. *Nat Neurosci* 16:227–234.
- Benda, J & Herz, V (2003). A universal model for spike-frequency adaptation. *Neural Comput* 15:2523–2546.
- Binzegger, T, Douglas, RJ, & Martin, KAC (2004). A quantitative map of the circuit of cat primary visual cortex. *J Neurosci* 39:8441–8453.
- Cabral, J, Kringelbach, ML, & Deco, G (2014). Exploring the network dynamics underlying brain activity during rest. *Prog Neurobiol* 114:102–131.
- Cichocki, A, Zdunek, R, Phan, AH, & Amari, Si (2009). *Nonnegative matrix and tensor factorizations: applications to exploratory multi-way data analysis and blind source separation*. (John Wiley & Sons).
- Cole, MW, Bassett, DS, Power, JD, Braver, TS, & Petersen, SE (2014). Intrinsic and task-evoked network architectures of the human brain. *Neuron* 83:238–251.

- de Kock, CPJ & Sakmann, B (2009). Spiking in primary somatosensory cortex during natural whisking in awake head-restrained rats is cell-type specific. *Proc Natl Acad Sci USA* 106:16446–16450.
- Deco, G & Jirsa, VK (2012). Ongoing cortical activity at rest: Criticality, multistability, and ghost attractors. *J Neurosci* 32:3366–3375.
- Eppler, JM, Pauli, R, Peyser, A, Ippen, T, Morrison, A, Senk, J, Schenck, W, Bos, H, Helias, M, Schmidt, M, et al. (2015). *Nest* 2.8.0.
- Felleman, DJ & Van Essen, DC (1991). Distributed hierarchical processing in the primate cerebral cortex. *Cereb Cortex* 1:1–47.
- Fourcaud, N & Brunel, N (2002). Dynamics of the firing probability of noisy integrate-and-fire neurons. *Neural Comput* 14:2057–2110.
- Goulas, A, Bastiani, M, Bezgin, G, Uylings, HB, Roebroek, A, & Stiers, P (2014). Comparative analysis of the macroscale structural connectivity in the macaque and human brain. *PLoS Comput Biol* 10:e1003529.
- Hilgetag, CC, Medalla, M, Beul, S, & Barbas, H (2015). The primate connectome in context: principles of connections of the cortical visual system. submitted.
- Jolivet, R, Rauch, A, Lüscher, HR, & Gerstner, W (2006). Predicting spike timing of neocortical pyramidal neurons by simple threshold models. *J Comput Neurosci* 21:35–49.
- Jones, E, Coulter, J, & Hendry, S (1978). Intracortical connectivity of architectonic fields in the somatic sensory, motor and parietal cortex of monkeys. *J Compar Neurol* 181:291–347.
- Jülich Supercomputing Centre (2015). JUQUEEN: IBM Blue Gene/Q<sup>®</sup> supercomputer system at the Jülich Supercomputing Centre. *Journal of large-scale research facilities* 1:1.
- Kuhn, A, Aertsen, A, & Rotter, S (2004). Neuronal integration of synaptic input in the fluctuation-driven regime. *J Neurosci* 24:2345–2356.
- Le Bon-Jego, M & Yuste, R (2007). Persistently active, pacemaker-like neurons in neocortex. *Front Neurosci* 1:123–129.
- Lorincz, ML, Gunner, D, Bao, Y, Connelly, WM, Isaac, JT, Hughes, SW, & Crunelli, V (2015). A distinct class of slow (0.2–2 Hz) intrinsically bursting layer 5 pyramidal neurons determines UP/DOWN state dynamics in the neocortex. *J Neurosci* 35:5442–5458.
- Magnus, JR & Neudecker, H (1995). *Matrix differential calculus with applications in statistics and econometrics*. (John Wiley & Sons).
- Markov, NT, Ercsey-Ravasz, M, Van Essen, DC, Knoblauch, K, Toroczkai, Z, & Kennedy, H (2013). Cortical high-density counterstream architectures. *Science* 342.

- Markov, NT, Ercsey-Ravasz, MM, Ribeiro Gomes, AR, Lamy, C, Magrou, L, Vezoli, J, Misery, P, Falchier, A, Quilodran, R, Gariel, MA, et al. (2014a). A weighted and directed interareal connectivity matrix for macaque cerebral cortex. *Cereb Cortex* 24:17–36.
- Markov, NT, Vezoli, J, Chameau, P, Falchier, A, Quilodran, R, Huissoud, C, Lamy, C, Misery, P, Giroud, P, Ullman, S, et al. (2014b). Anatomy of hierarchy: Feedforward and feedback pathways in macaque visual cortex. *J Compar Neurol* 522:225–259.
- Morel, A & Bullier, J (1990). Anatomical segregation of two cortical visual pathways in the macaque monkey. *Visual neuroscience* 4:555–578.
- Morrison, A, Diesmann, M, & Gerstner, W (2008). Phenomenological models of synaptic plasticity based on spike-timing. *Biol Cybern* 98:459–478.
- Neske, GT, Patrick, SL, & Connors, BW (2015). Contributions of diverse excitatory and inhibitory neurons to recurrent network activity in cerebral cortex. *J Neurosci* 35:1089–1105.
- Ostojic, S, Brunel, N, & Hakim, V (2009). How connectivity, background activity, and synaptic properties shape the cross-correlation between spike trains. *J Neurosci* 29:10234–10253.
- Perkel, DJ, Bullier, J, & Kennedy, H (1986). Topography of the afferent connectivity of area 17 in the macaque monkey: A double-labelling study. *J Compar Neurol* 253:374–402.
- Pernice, V, Staude, B, Cardanobile, S, & Rotter, S (2011). How structure determines correlations in neuronal networks. *PLoS Comput Biol* 7:e1002059.
- Plesser, HE & Diesmann, M (2009). Simplicity and efficiency of integrate-and-fire neuron models. *Neural Comput* 21:353–359.
- Potjans, TC & Diesmann, M (2014). The cell-type specific cortical microcircuit: Relating structure and activity in a full-scale spiking network model. *Cereb Cortex* 24:785–806.
- Rauch, A, La Camera, G, Lüscher, H, Senn, W, & Fusi, S (2003). Neocortical pyramidal cells respond as integrate-and-fire neurons to in vivo like input currents. *J Neurophysiol* 90:1598–1612.
- Rockland, KS & Pandya, DN (1979). Laminar origins and terminations of cortical connections of the occipital lobe in the rhesus monkey. *Brain Res* 179:3–20.
- Salin, PA & Bullier, J (1995). Corticocortical connections in the visual system: structure and function. *Physiol Rev* 75:107–154.
- Sanchez-Vives, MV & McCormick, D (2000). Cellular and network mechanisms of rhythmic recurrent activity in neocortex. *Nat Neurosci* 3:1027–1034.
- Scannell, JW, Grant, S, Payne, BR, & Baddeley, R (2000). On variability in the density of corticocortical and thalamocortical connections. *Phil Trans R Soc B* 355:21–35.

- Schmidt, M, Bakker, R, Shen, K, Bezgin, G, Diesmann, M, & van Albada, SJ (2015a). Full-density multi-scale account of structure and dynamics of macaque visual cortex. arXiv preprint arXiv:1511.09364.
- Schmidt, M, Schuecker, J, Diesmann, M, & Helias, M (2015b). Shaping phase space of neural networks via connectivity. In Proceedings of the 11th Göttingen Meeting of the German Neuroscience Society p. T26 7C.
- Schmitt, O, Eipert, P, Kettlitz, R, Leßmann, F, & Wree, A (2014). The connectome of the basal ganglia. *Brain Structure and Function* pp. 1–62.
- Seltzer, B & Pandya, DN (1991). Post-rolandic cortical projections of the superior temporal sulcus in the rhesus monkey. *J Compar Neurol* 312:625–640.
- Seltzer, B & Pandya, DN (1994). Parietal, temporal, and occipital projections to cortex of the superior temporal sulcus in the rhesus monkey: A retrograde tracer study. *J Compar Neurol* 343:445–463.
- Shen, K, Hutchison, RM, Bezgin, G, Everling, S, & McIntosh, AR (2015). Network structure shapes spontaneous functional connectivity dynamics. *J Neurosci* 35:5579–5588.
- Stephan, K, Kamper, L, Bozkurt, A, Burns, G, Young, M, & Kötter, R (2001). Advanced database methodology for the collation of connectivity data on the macaque brain (CoCoMac). *Phil Trans R Soc B* 356:1159–1186.
- Strogatz, SH (1994). *Nonlinear Dynamics and Chaos: with Applications to Physics, Biology, Chemistry, and Engineering*. (Reading, Massachusetts: Perseus Books).
- Suzuki, WL & Amaral, DG (1994). Perirhinal and parahippocampal cortices of the macaque monkey: cortical afferents. *J Compar Neurol* 350:497–533.
- Swadlow, HA (1988). Efferent neurons and suspected interneurons in binocular visual cortex of the awake rabbit: Receptive fields and binocular properties. *J Neurophysiol* 59:1162–1187.
- Tomioka, R & Rockland, KS (2007). Long-distance corticocortical GABAergic neurons in the adult monkey white and gray matter. *J Compar Neurol* 505:526–538.
- Trousdale, J, Hu, Y, Shea-Brown, E, & Josic, K (2012). Impact of network structure and cellular response on spike time correlations. *PLoS Comput Biol* 8:e1002408.
- Turrigiano, GG, Leslie, KR, Desai, NS, Rutherford, LC, & Nelson, SB (1998). Activity-dependent scaling of quantal amplitude in neocortical neurons. *Nature* 391:892–896.
- van Albada, SJ, Helias, M, & Diesmann, M (2015). Scalability of asynchronous networks is limited by one-to-one mapping between effective connectivity and correlations. *PLoS Comput Biol* 11:e1004490.
- Van Essen, DC (2002). Windows on the brain: the emerging role of atlases and databases in neuroscience. *Curr Opin Neurobiol* 12:574–579.

- Van Essen, DC, Drury, HA, Dickson, J, Harwell, J, Hanlon, D, & Anderson, CH (2001). An integrated software suite for surface-based analyses of cerebral cortex. *Journal of the American Medical Informatics Association* 8:443–459.
- van Kerkoerle, T, Self, MW, Dagnino, B, Gariel-Mathis, MA, Poort, J, van der Togt, C, & Roelfsema, PR (2014). Alpha and gamma oscillations characterize feedback and feedforward processing in monkey visual cortex. *Proc Natl Acad Sci USA* 111:14332–14341.
- van Vreeswijk, C & Sompolinsky, H (1996). Chaos in neuronal networks with balanced excitatory and inhibitory activity. *Science* 274:1724–1726.
- Voorhees, EM (1986). Implementing agglomerative hierarchic clustering algorithms for use in document retrieval. *Information Processing & Management* 22:465–476.
- Wedeen, VJ, Wang, R, Schmahmann, JD, Benner, T, Tseng, W, Dai, G, Pandya, D, Hagmann, P, D’Arceuil, H, & de Crespigny, AJ (2008). Diffusion spectrum magnetic resonance imaging (ds) tractography of crossing fibers. *NeuroImage* 41:1267–1277.
- Wong, KF & Wang, XJ (2006). A recurrent network mechanism of time integration in perceptual decisions. *J Neurosci* 26:1314–1328.